Journal of Molecular Structure 1333 (2025) 141790

Contents lists available at ScienceDirect

Journal of Molecular Structure

journal homepage: www.elsevier.com/locate/molstr

Synthesis, characterization of europium(III) and terbium(III) complexes containing lawsone ligand and their interaction with DNA, HSA, and topoisomerases

Josias S. Rocha [a,*], George B.S. Pereira [a], Marcos V. Palmeira-Mello [a], Willyan F. Oliveira [d], Jocely L. Dutra [a], Tamara Teixeira [a], Nádija N.P. da Silva [a], Gabriela P. Oliveira [a], Paulo C. Gomes-Junior [a], Anna C.S.J. Passaes [e], João H. Araujo-Neto [c], Alzir A. Batista [a], Javier Ellena [b], José D.L. Dutra [d], Renan L. Farias [e], Fillipe V. Rocha [a,*]

[a] Departamento de Química, Universidade Federal de São Carlos, São Carlos, São Paulo, CEP 13565-905, São Carlos, São Paulo, Brazil
[b] Instituto de Física de São Carlos, Universidade de São Paulo, São Carlos, São Paulo, CEP 13566-590, São Carlos, São Paulo, Brazil
[c] Departamento de Química Fundamental, Instituto de Química, Universidade de São Paulo, 05508-000, São Paulo, São Paulo, Brazil
[d] Pople Computational Chemistry Laboratory, Departamento de Química, Universidade Federal de Sergipe, CEP 49100-000, São Cristóvão, Sergipe, Brazil
[e] Department of Chemistry, Pontifical Catholic University of Rio de Janeiro, Brazil

ARTICLE INFO

Keywords:
Bioinorganic chemistry
DNA
Anticancer agents
Lawsone
Europium and terbium

ABSTRACT

In this study, two complexes based on Europium $[Eu(LAW)_3(H_2O)_3]$ **(1)** and Terbium $[Tb(LAW)_3(H_2O)_3]$ **(2)**, each containing the lawsone ligand, were synthesized and comprehensively characterized using Infrared and UV-Visible spectroscopies, Cyclic Voltammetry, Conductivity, and Magnetic Susceptibility measurements. Crystal structure information was determined via X-ray diffraction (XRD), and elemental analysis confirmed the compounds' purity. Experimental and theoretical UV-Vis data were compared through TD-DFT calculations, providing insights into the low luminescence of both Eu(III) and Tb(III) complexes, with excited states calculated both with and without solvent effects. DNA-binding experiments with ct-DNA were conducted using viscosity measurements, UV-Vis titrations, circular dichroism, and fluorescence competition assays to explore the complexes' primary interactions with the DNA target. Additionally, DNA cleavage properties were examined using pBR322 plasmid DNA with agarose gel electrophoresis. Although no cleavage activity was observed, DNA interaction studies suggested covalent binding, supported by viscosity and circular dichroism data. Furthermore, analyzing the docking results, both compounds demonstrated stable conformations within the Sudlow I site also the lawsone-based compounds demonstrated an ability to bind to human serum albumin (HSA) with binding constants (K_b) in the range of 10^5-10^6 and showed Topoisomerase IIα inhibition at 50 μM. Both compounds remained stable for up to 48 hours.

1. Introduction

After the discovery of the anti-tumor properties of cisplatin, the bioinorganic field became a crucial area dedicated to developing new complexes with high cytotoxicity and less toxicity than conventional platinum-based complexes [1]. The f-block metals or lanthanides have been studied in this scenario due to their promising anticancer properties. They are being quoted as the new generation of metal complexes with chemotherapeutic and therapeutic properties [2–4].

The success of these metal-based compounds may be due to their similarity to bioessential metals such as calcium, zinc, iron, and manganese. Another similarity of the lanthanides is their ionic radii are close to that of calcium, 85-106 and 86 pm respectively, and a high charge originating from these metals when in the form of salt (Ln^{+3}), which makes it necessary to coordinate them with stable ligands since their free salts can be toxic to humans due to the possible inhibition of cellular events provided by Ca^{2+}. In addition to their similar ionic radii, lanthanides share characteristics with calcium, such as flexible electrostatic bonding and a strong preference for coordinating with oxoanions [5]. In addition, these metals and complexes have been receiving attention not

* Corresponding authors.
E-mail addresses: josias.rocha@estudante.ufscar.br (J.S. Rocha), fillipe@ufscar.br (F.V. Rocha).

https://doi.org/10.1016/j.molstruc.2025.141790
Received 11 November 2024; Received in revised form 14 February 2025; Accepted 17 February 2025
Available online 18 February 2025

only in disease diagnostic areas but also in the combat of cancer, in the application of photodynamic therapy (PDT), biosensors, drug delivery, and in the development of highly cytotoxic complexes against various tumor cells [4,6].

One of the remarkable properties of europium-based complexes is their intense luminescence, which arises from the unique electronic structure of the Eu(III) ion. These complexes exhibit sharp emission bands with long lifetimes due to the efficient intramolecular energy transfer from the coordinated ligands to the metal center, a phenomenon known as the "antenna effect." This characteristic makes europium complexes highly attractive for bioimaging applications, luminescent probes, and diagnostic tools. Moreover, their photophysical stability and ability to provide a high signal-to-noise ratio in fluorescence assays further enhance their potential in biomedical applications, particularly in drug delivery and targeted therapies [2,3].

Studying DNA and topoisomerase enzymes is essential for developing effective cancer treatments. DNA serves as a key molecular target for numerous anticancer drugs, as it is directly involved in cell survival and proliferation. Topoisomerases, on the other hand, play a critical role in the cell cycle and DNA replication processes, making them vital for cancer cell growth. Inhibiting these enzymes can disrupt DNA replication and cell division, leading to cell death and providing a targeted approach to treat cancer. [2,7].

Lawsone (2-hydroxy-1,4-naphthoquinone) has been explored for medicinal purposes due its several biological properties such as anticancer, antimicrobial, antiproliferative, antiparasitic and many others [7]. These medicinal properties arise from the presence of quinone moiety and its conversion into semiquinone or hydroquinone upon one or two reductions in biological medium. In general, lawsone and other quinone derivatives can form stable complexes with d block metals, such as Zn, Co, Mn, Cu, Ni, and Ru [8–11], exhibiting promising cytotoxic activities and several mechanisms of action.

In this context, the work of Chen *et al.* stands out, involving Yttrium (III), Lanthanum(III), Samarium(III), Gadolinium(III), and Dysprosium (III) complexes with Plumbagin-type ligands (5-hydroxy-2-methyl-1,4-naphthoquinone, H-PLN). These complexes demonstrated inhibitory capacity against cell types such as BEL7404(Human liver cancer cell) [12,13]. Despite these promising results, there are still few works with Europium and Terbium based on naphthoquinones.

In this study, we report the synthesis and characterization of two novel complexes, Eu-Lawsone $[Eu(LAW)_3(H_2O)_3]$ (**1**) and Tb-Lawsone $[Tb(LAW)_3(H_2O)_3]$ (**2**). To explore their potential biological applications, we investigated the DNA binding properties of these complexes using a combination of analytical techniques, including UV-Vis spectroscopy, fluorescence spectroscopy, circular dichroism (CD), viscosity measurements, and agarose gel electrophoresis. Collectively, these methods provided insight into the interaction mechanisms between the complexes and DNA.

Given the well-documented ability of quinone compounds to act as topoisomerase inhibitors [14], we further evaluated complexes **1** and **2** for their inhibitory effects on topoisomerase IIα (topo IIα) and topoisomerase Iβ (topo Iβ) enzymes. The aim of this investigation was to evaluate their potential as anticancer agents, since topoisomerase inhibition is a key mechanism for disrupting DNA replication and inducing cell death in cancer cells. In addition, we evaluated their interaction with human serum albumin (HSA) to assess their drug transport capabilities and pharmacokinetic behavior. These findings underscore the potential of complexes **1** and **2** for further development in medicinal chemistry.

2. Materials and methods

2.1. General methods

The reagents and the solvents were purchased as reagent-grades from Acros, Sigma–Aldrich, and Synth, and they were used without any further purification. Conductivity data was obtained using 10^{-3} M solutions of the complex in DMSO, at room temperature, using a MARCONI instrument MA521 model. The IR spectra were recorded on a FT-IR SHIMADZU IRTracer-100 spectrometer in the range 4000-200 cm^{-1} by using CsI pellets. Electrochemical measurements were performed using a three-electrode single-compartment glass cell containing an Ag|AgCl|KCl (3.0 mol L^{-1}) reference electrode, a platinum plate as a counter electrode, and bare GCE ($\phi = 3.0$ mm) as the working electrode. Cyclic voltammetry (CV) was performed using an μAutolab μsAUT71003 (Eco Chemie, Utrecht, the Netherlands) potentiostat/galvanostat Type 3. The measurements of the effective magnetic moment (μef) were performed on a Johnson Mattey-AUTO MSB scale. The electronic spectra of UV-Vis were obtained in DMSO and RPMI (Culture medium) on a SHIMADZU-1650PC spectrophotometer. The emission spectra were obtained using a Shimadzu model RF-5301 PC spectrofluorimeter - 150 W xenon high 150 W xenon lamp and R928 photomultiplier and four-sided quartz cuvettes with an optical path of 10 mm and a volume of 3.5 mL were used. volume 3.5 mL in DMSO.

2.2. X-Ray diffraction

A single crystal of the complex was obtained, suitable for X-ray diffraction analysis. X-ray diffraction data were collected at 298 K on a Rigaku XtaLAB mini diffractometer using MoKα radiation ($\lambda = 0.71073$ Å) with graphite monochromator. Structural solution was achieved via direct phase retrieval with SHELXT, followed by refinement through full-matrix least squares using SHELXL [15], all within the OLEX2 software environment Non-hydrogen atoms were refined anisotropically, while hydrogen atoms were placed in calculated positions and refined in riding mode [15]. Mercury software was employed for artwork preparation and structural analysis [16]. Crystallographic data and refinement parameters are provided in Table S3. A solvent mask was applied to account for the electron density attributed to three water molecules in the structure. This mask, calculated using the “solvent mask” procedure within the OLEX2 software, revealed an electron density of 130 electrons occupying a volume of 658 $Å^3$ within a single void per unit cell. This finding aligns with the presence of three water molecules per formula unit, which corresponds to an approximate electron count of 120 per unit cell. This approach enabled accurate refinement by compensating for unmodeled solvent electron density [17].

2.3. TD-DFT and LUMPAC simulations

Since the crystallographic structures for both complexes were obtained, these structures were used as the starting point for the geometry optimization calculations. The optimizations were carried out using the ORCA5.0.4 software [18] with the DFT approach, where the hybrid functional PBE1PBE and the TZVP basis set were considered for both complexes. To represent the central lanthanide ions, the effective core potentials (ECP) MWB52 and MWB54 were used for the Eu^{3+} and Tb^{3+} ions, respectively. The MWB52 ECP treats the 52 core electrons of the Eu^{3+} ion as an electrostatic potential, similarly to how the MWB54 ECP treats the 54 core electrons of the Tb^{3+} ion. Thus, the PBE1PBE/TZVP/MWB52 level of theory was applied to complex **1** and PBE1PBE/TZVP/MWB54 to complex **2**. To evaluate the effect of including long-range interactions and the solvent effect in the structural modeling of both complexes, the dispersion coefficients D3 and D4, as well as the implicit effect of the DMSO solvent, were considered in the calculations. The D3 and D4 models efficiently include long-range electronic interaction correlations, allowing for the consideration of London dispersion interactions, for example [19]. The DMSO solvent was considered in the calculations using the Conductor Polarized Continuum Model (CPCM) [20], where the solvent effect is treated implicitly through the dielectric constant surrounding the structure, with boundaries determined by the van der Waals spheres of each atom. A dielectric

constant of 47.2 was used for the DMSO solvent in ORCA5.0.4. The CAM-B3LYP/TZVP/MWB52 and CAM-B3LYP/TZVP/MWB54 methods for complexes **1** and **2**, respectively, were used to calculate the excited states with and without the inclusion of the solvent effect. To investigate the low luminescence of the complexes, a theoretical study was conducted focusing on the ligand-Ln^{3+}. Energy transfer processes were investigated using models to quantify the energy transfer rates proposed by Malta [21,22] implemented in LUMPAC [23]. This is a well-established approach that has been applied in several studies [24–31].

2.4. HSA computational methodology

The crystal structure of Human Serum Albumin (HSA), with a resolution of 3.05 Å, co-crystallized with warfarin (WAR) in Sudlow I binding site was obtained from the Protein Data Bank (PDB ID: 2BXD) [32]. Subsequently, the missing residues were reconstructed (**Fig. S12**) using the Swiss-PDB Viewer software (v4.1.0) [33]. The protein structure quality was assessed by analyzing the Ramachandran plot (**Fig. S13**). The computational method was validated by redocking the WAR ligand to determine the induced-fit docking parameters. In CSD GOLD software [34], the interaction sphere radius was set as 16 Å, with 100 runs performed for each ligand. A semi-flexible molecular docking protocol was applied to preserve the active conformation of the HSA. The resulting poses were ranked using the ChemScore scoring function, which showed the best correlation between its score and the ability of the software to correctly reposition the simulated WAR in the experimental one, with a root-mean-square deviation (RMSD) below 2 Å. Subsequently, the same routine was applied to the complexes of interest, previously minimized using the semi-empirical PM7 method. Finally, all graphical representations of the complexes were analyzed using the Discovery Studio Visualizer (DSV) [35].

2.5. Interaction with DNA

2.5.1. Spectrophotometric titrations with ct-DNA

5mg of ct-DNA (Calf thymus) was dissolved in 5mL of Trisma buffer (pH = 7.4, aqueous solution of 1.0 x 10^{-3} M tris-HCl, 1.0 x 10^{-3} M NaCl). The solution was left in the fridge for a day to facilitate DNA dissolution. Prior to analysis, the absorbance of the ct-DNA stock solution was measured, and its concentration determined, since the molar absorptivity is already known in the literature ($\varepsilon = 6600\ L\ mol^{-1}\ cm^{-1}$; λ = 260 nm) and the Lambert-Beer law was applied the concentration was then found and diluted to 1.0 x 10^{-3} M. In this experiment, the concentration of the complexes was kept fixed at 1.0 x 10^{-5} M, where the concentrations of DNA were varied from 1.0 x 10^{-6} – 2.0 x 10^{-5} M, it is worth noting that the additions of DNA were made to both the working cuvette and the blank to eliminate the absorbance of the biomolecule. Finally, the changes in the bands were monitored at λ= ~450 nm [36]. The binding constant (K_b) was calculated using the Benesi-Hildebrand equation (Eq. (1)), where, [DNA] is the added concentration of DNA, $\varepsilon_A = A_{obs}/[complex]$, ε_f is the molar absorptivity coefficient of the free compound and ε_b is the molar absorptivity coefficient of the compound bound to DNA.

$$\frac{[DNA]}{\varepsilon_A - \varepsilon_f} = \frac{[DNA]}{\varepsilon_b - \varepsilon_f} + \frac{1}{K_b(\varepsilon_b - \varepsilon_f)}$$

2.5.2. Viscosity assays

The viscosity experiments were carried out by using an Ostwald viscosimeter maintained in a thermostatic bath at 25 °C. The samples (4.0 mL) were prepared in Tris-HCl buffer (pH 7.4) containing 20 % of DMSO. The ct-DNA concentration was kept constant at 100 μM, and the concentrations of complexes were varied, to obtain different molar ratios, [Complex]/[ct-DNA] (0.05 – 0.50). The flow times were recorded with a digital stopwatch, in five replicates. The specific viscosity values $(\eta/\eta_0)^{1/3}$ were plotted *versus* [complex]/[ct-DNA], where η and η_0 correspond to the relative viscosity of DNA in the presence and the absence of the complexes, respectively. Eq. (1) was used to calculate the relative viscosity of DNA (η_0) values from the flow time of the DNA solution (t) corrected for the flow time of the buffer (t_0) [37].

$$\eta_0 = \frac{(t - t_0)}{t_0} \quad (1)$$

2.5.3. Circular dichroism

The CD titrations were carried out with a JASCO J-815 spectropolarimeter at 25 °C. Solutions of ct-DNA (100 μM) in Tris-HCl buffer (pH 7.4) with different molar ratios [Complex]/[ct-DNA] (0.05–0.5) were incubated at 37 °C for 24 h. The spectra of these solutions were recorded from 230 to 500 nm using a quartz cuvette with an optical path length of 0.5 cm and a scanning rate of 200 nm min^{-1} and obtained after 5 accumulations [36].

2.5.4. Competitive displacement assay with Hoechst 33258

The concentration of Hoechst 33258 and DNA was determined by UV-Vis. The Hoechst concentration was calculated using the absorbance value and the molar absorptivity of Hoechst at 344nm (ε= 46000 cm^{-1} mol^{-1} L) and the optical path (b = 1cm), according to the Lambert-Beer law: $A = \varepsilon \times b \times C$. Subsequently, 10 mL of a DNA-Hoechst stock solution was prepared in Trisma-HCl with concentrations of 100 μM of DNA and 5.0 μM of Hoechst. Increasing aliquots (5 – 40μL) of the complexes in DMSO were added to different microtubes of 1500μL, and the volume of DMSO was topped up to 100μL (10 %). Next, 900μL of the DNA-Hoechst stock solution was transferred to each microtube, making a total volume of 1000 μL. In one of the microtubes, only DMSO was added in the absence of the complexes and the DNA-Hoechst stock solution. The solutions were incubated at 25 °C for 30 min. Three aliquots of 200 μL from each microtube were transferred to three wells of an opaque 96-well plate, and the measurements were carried out in triplicate. The fluorescence emission spectra were obtained using a Synergy/H1-Biotek monochromator fluorimeter, at 25°C, with excitation at 340nm and recorded in the 370 to 700 nm region [38].

2.5.5. Competitive displacement assay with TO

The competitiveness test using Thiazole Orange (TO) was carried out by means of TO (2.5 μM)/ct-DNA (75 μM) fluorescence suppression experiments in Trizma buffer (pH=7.4). The extinction of the TO/DNA emission intensity at 530 nm (excitation wavelength 480 nm) was monitored using the complexes, at different concentrations (0; 3.5; 7.0; 10.5; 14.0; 17.5; 21.0; 24.5 and 28 μM), dissolved in DMSO (10 %), with the quencher. The experiment was carried out in triplicate using opaque 96-well plates. The fluorescence experiment was carried out using a Synergy H1 Multi-Mode Reader (BioTek) [38].

2.5.6. Agarose gel electrophoresis

For the tests, the complexes were first diluted in three concentrations, 100, 10 and 1 μM, then in a microtube, 1 μL of these solutions were added to a solution containing 27 μL of deionized water and 3 μL of the pUC19 plasmid, giving a final test volume of 30 μL. The solutions were incubated at 37 °C for 24 hours. After the time had elapsed, the samples were removed from the thermostatic bath and 15 μL of STEB (40 % sucrose, 100 mmol.L-1 Tris.HCl, pH = 7.5, 1 mM EDTA, 0.5 mg mL-1 bromophenol blue) were added, then centrifuged and 20 μL of the samples were added to the respective wells of the 1 % agorose gel (525 mg of agarose in 53 mL of 1x TBE). The electrophoretic run took place in 1x TBE solution at 60 V for 2 hours. After this period, the gel was added to ethidium bromide stained solution and developed in the Gel DocTM EZ photodocumenter, the image obtained was processed using Image-LabTM 6.0.0 software provided by BioRad [36].

2.5.7. Interaction with human serum albumin (HSA)

Initially, a stock solution of HSA at 5.25 μM was prepared by solubilizing 17.5 mg of HSA in 50 mL of Trisma-HCl buffer. The concentration of the HSA stock solution was determined by UV-vis, using the molar absorptivity value of HSA at 280 nm. Subsequently, aliquots of 0 – 30 μL of the stock solutions of the complexes (concentration of 1.0 x 10^{-3} M) were added to a 2 mL microtube, followed by the addition of aliquots of 0 – 50 μL dimethylsulfoxide (The sum of the volumes of the aliquots makes a total volume of 50 μL). After, 950 μL of the albumin stock solution (5.25 μM) was added to the complex solutions. Therefore, solutions (1 mL) of the HSA protein were prepared with different molar concentrations of the complexes in Trisma-HCl (5% DMSO), keeping the albumin concentration constant at 5 μM. The molar concentrations of the complexes were 0, 5, 10, 15, 20, 25 and 30 μM. The HSA solution in Trisma-HCl buffer (5 % DMSO) was used as a negative control. Solutions of the complexes in Trisma-HCl buffer (5 % DMSO), at the highest concentrations used (30 μM), were used to verify the absence of fluorescence emission from the complexes. Immediately after preparing the HSA/complex solutions, four 200 μL aliquots of each solution were added to four wells (200 μL/well) of an opaque 96-well plate. In this way, quadruplicate measurements of the solutions were made. After plating the solutions, the fluorescence emission spectra were recorded in the 300 to 700 nm region, with an excitation length of 270 nm. The measurements were carried out at temperatures of 298, 303 and 310 K. The experiments were carried out on a Synergy/H1-Biotek monochromator fluorimeter using an opaque 96-well plate [37,38].

2.5.8. Topoisomerase IIα and Iβ interaction: relaxation assay

The DNA-Topoisomerase IIα enzyme inhibition assay was carried out using the DNA relaxation kit supplied by Inspiralis Limited. The assay used 0.5 μL of DNA (pBR322), 3 μL of buffer (Tris.HCl 4.5 x 10^{-3} mol L^{-1}, 5.0 x 10^{-4} mol L^{-1} Tris. base and 5.0 x 10^{-2} mol L^{-1} NaCl pH 7.4) and 1μL (1.0 x 10^{-3} mol L^{-1}) of ATP to prepare the mix. The test solution consisted of 4.5 μL of mix, 23 μL of water, 3.0 μL of the complexes and, finally, 1 μL of topo II. The complexes were tested at different concentrations (10.0, 5.0, 1.0 and 0.1 μmol L^{-1}). To carry out the assay, the samples were incubated at 37 °C for 45 minutes. After this period, 15μL of STEB (40 % sucrose, 100 mM Tris.HCl, pH = 7.4, 1.0 x 10^{-3} mol L^{-1} EDTA, 0.5 mg mL^{-1} bromophenol blue) was added. The samples were centrifuged at 5000 rpm for 20 seconds from the supernatant, 20 μL of the aqueous phase was added to the 1 % agarose gel in 1x TBE buffer (Tris/Borate/EDTA) pH = 7.2. The electrophoretic run was carried out at 60 V for 2 hours. The gel was developed, and the images processed in the same way as described above. The electrophoretic assay with the Topoisomerase Iβ enzyme followed the same protocol described for Topoisomerase IIα, without adding ATP to the mix [39].

2.6. Syntheses of complexes

Lawsone (for **1**, 0.819 mmol, 143 mg; for **2**, 0.804 mmol, 140 mg) was dissolved in 5 mL of ethanol, and 0.200 μL of the NH_4OH was added. After a few minutes, until the smell of ammonia disappeared, the $LnCl_3 \cdot 6H_2O$ salt (for **1**, 0.273 mmol, 0.100 mg; for **2**, 0.268 mmol, 0.100 mg) pre-dissolved in a small amount of ethanol was added to the solution, and the reaction changed from red to dark brown. The reaction was left to reflux for 2 hours and overnight at room temperature. The precipitate was filtered, washed with ethanol and water and dried under reduced pressure.

2.6.1. [Eu(LAW)$_3$(H$_2$O)$_3$].5H$_2$O (1)

Yield: 97 %. μ_{eff}: 7.9μ_B at 298 K. Molecular conductance (Λ_M) in DMSO at 298 K: 19.40 $Scm^2.mol^{-1}$. $C_{30}H_{21}EuO_{12}\cdot(H_2O)_6$: Found (Cal.) %: C = 43.98 (43.23); H = 4.01 (3.99).

2.6.2. [Tb(LAW)$_3$(H$_2$O)$_3$].7H$_2$O (2)

Yield: 82 %. μ_{eff}: 9.4μ_B at 298 K. Molecular conductance (Λ_M) in DMSO at 298 K: 17.34 Scm^2 mol^{-1}. $C_{30}H_{21}O_{12}Tb\cdot(H_2O)_4$: Found (Cal.) %: C = 44.95 (44.79); H = 3.62 (3.63).

3. Results and discussions

3.1. General characterization

The syntheses of the complexes were adapted from the literature [40–42]. In 3:1 (LAW:Ln^{3+}) proportions, the lawsone (LAW) ligand was first deprotonated to favor coordination. Both complexes were obtained as a dark brown powder (**Scheme S1**).

The formation of complexes was confirmed by several techniques, such as ultraviolet-visible, infrared, CHN, and single-crystal X-ray diffraction. One of the more significant evidence for the coordination of the three lawsone ligands is the conductivity values, which show them to be non-electrolyte due to the 3+ nox of the salts being offset by the negative charge of each ligand after deprotonation [43]. Another characteristic of the formation of quinone-based complexes is the appearance of a broad band in the 400-500 nm range (**Fig. S1**), characteristic of n-π* transitions [10]. In addition, it was possible to note the appearance of a transition from F levels to D at approximately 650 nm.

Cyclic Voltammetry (CV) also evidenced complexation, comparing the ligand's potential with its respective complexes (Fig. 1, and **Fig. S2**). The voltammetric profile of LAW showed two well-defined peaks with anodic (E_{ap}) and cathodic (E_{cp}) potentials at 1.03 and −0.71 V, respectively (Fig. 1A). However, when the ligand complexes with europium, E_{ap} and E_{cp} shift to 0.81 and −0.45 V, representing 220 and 170 mV of variation (Fig. 1B). Similarly, when LAW complexes with terbium, E_{ap} and E_{cp} are shifted to 0.85 and −0.40 V, representing 180 and 310 mV of variation, respectively (**Fig. S2**).

Infrared spectrometry was used to monitor the characteristic stretches of the lawsone ligand (**Fig. S3**) compared to its europium and terbium complexes. Bands diagnostic of νC=O in the ligand appear at 1643 and 1680 cm^{-1} for the carbonyl of the keto-enol equilibrium and the carbonyl trans to it, respectively (Table S1). The νC-O stretch (hydroxyl) in the free lawsone appears at 982 cm^{-1}. After coordination, shifts and significant decreases in the intensities of the carbonyl bands are observed, especially for complex **2** (**Fig. S3**). Although they do not show substantial shifts, it is possible to observe decreases in the transmittance of these bands. This observation aligns with a decrease in the C=O bond order due to coordination with the metal, as confirmed by X-ray diffraction. For instance, in the terbium complex, the C=O bond distance (C1–O1) is 1.221 Å (**Tables S1 and S2**), slightly longer than in the free Lawsone ligand, which has a distance of 1.212 Å [44,45]. The νC=O stretching frequency also shifts to higher energy, indicating a post-coordination resonance effect. Both complexes exhibit a broad spectral range (**Fig. S1**), with the νOH stretch observed between 3500–3000 cm^{-1}, indicating the presence of coordinated and crystallization water, which was confirmed in the terbium complex crystal and accounted for in the elemental analysis (see synthetic methodology of the complexes). Additional characteristic stretches of the ligand and its complexes are listed in **Table S1**.

3.2. Single-crystal diffraction (X-ray)

Recently, in distinct works, Gonçalves and collaborators published an identical single-crystal structure of the europium complex containing lawsone ligands, where they explored all the thermal and redox properties of the complex in addition to the single-crystal structure [45]. In this case, the present work will present the single-crystal structure of the analogous terbium complex (Fig. 2), which differs only (apart from the coordination center) by the crystallization of water molecules outside the coordination sphere. The crystal data of diffraction was presented in Table 1.

The crystals were obtained by slowly evaporating the mother solution after filtration, and the formation of red crystals was observed in

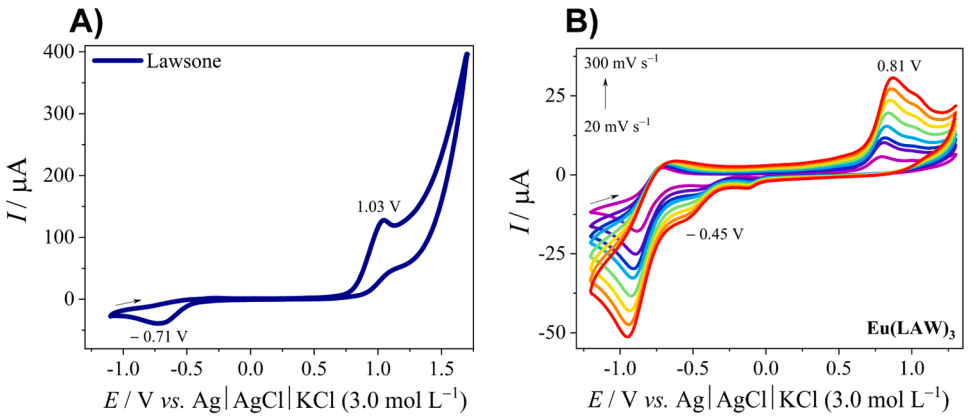

Fig. 1. Cyclic voltammograms obtained at different scan rates (20 – 300 mV s^{-1}) for the ligand (A), and complex 1 (B) in DMF using GCE in 0.1 mol L^{-1} tertabutylammonium perchlorate (TBAP) as supporting electrolyte at 298K.

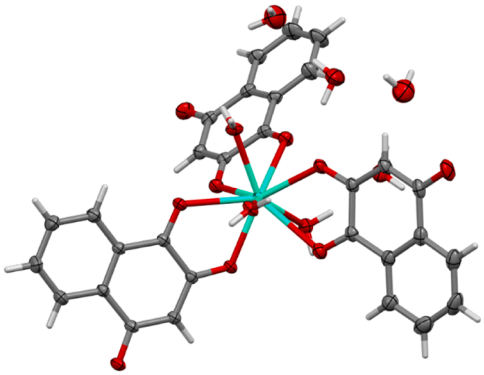

Fig. 2. Single-crystal structure for the $[Tb(LAW)_3(H_2O)_3](H_2O)_7$ (complex 2). CCDC 2397855.

Table 1
Crystal data and structure refinement for $[Tb(LAW)_3(H_2O)_3].(H_2O)_4$ (complex 2).

CCDC number	2397855
Asymmetric Unity content	$Tb(Law)_3(H_2O)_3$
Empirical formula	$C_{30}H_{35}O_{19}Tb$
Formula weight	858.526
Temperature/K	293(2)
Crystal system	monoclinic
Space group	$P2_1/c$
a/Å	16.5351(7)
b/Å	29.7091(12)
c/Å	7.3771(3)
α/°	90
β/°	93.431(4)
γ/°	90
Volume/$Å^3$	3617.5(3)
Z	4
$\rho_{calc}g/cm^3$	1.576
μ/mm^{-1}	2.033
F(000)	1729.5
Crystal size/mm^3	0.364 × 0.28 × 0.188
Radiation	Mo Kα (λ = 0.71073)
2Θ range for data collection/°	5.12 to 51.36
Index ranges	$-25 \leq h \leq 26$, $-46 \leq k \leq 47$, $-11 \leq l \leq 11$
Reflections collected	59921
Independent reflections	6853 [$R_{int} = 0.0437$, $R_{sigma} = 0.0457$]
Data/restraints/parameters	6853/0/443
Goodness-of-fit on F^2	1.091
Final R indexes [I>=2σ (I)]	$R_1 = 0.0291$, $wR_2 = 0.0579$
Final R indexes [all data]	$R_1 = 0.0351$, $wR_2 = 0.0625$

about three days. The terbium complex has nine coordination points, with three lawsone ligands coordinated via carbonyl and deprotonated oxygen and three water molecules coordinated via oxygens. The distances in the coordinated lawsone ligand are characterized by the difference in the bond distances of the respective oxygens, due to deprotonation and the liquid negative charge, the hydroxyl oxygens have longer bond distances, from 2.314 to 2.343 Å (**Table S2**), values consistent with the analogous structure already published [45], other values such as bond distances, unit cells is presented in the supplementary material (**Fig. S4**). The crystallographic data is presented in the Table 1.

Using Crystal Explorer, non-covalent interactions were identified from the Hirshfeld surface (HS) analysis. Strong intermolecular interactions appear as red spots on the Hirshfeld surface (Fig. 3A). Projecting the Hirshfeld surface onto a two-dimensional graph with parameters de (y-axis) and di (x-axis) enabled quantification of interatomic contact contributions to crystal packing. For the $Tb(LAW)_3$ (2) compound, the primary contributions are H···H (43.1 %), O···H (25.8 %), and C···H (18.6 %), as illustrated in Fig. 3B. Weaker intermolecular interactions, including C···C (7.8 %) and C···O (4.3 %), contribute less significantly to crystal packing.

From the Hirshfeld surface, it was possible to identify some intermolecular interactions that contribute significantly to the packing of the crystal (Fig. 4A). The coordinated water molecule acts as a hydrogen atom donor. It establishes intermolecular bonds with the oxygen of the adjacent molecule, providing O(1W)-H(1WA)•••O(4B) intermolecular interactions with a bond length of 2.0190(23)Å and angle of 156.7°. Also observed are C(3B)-H(3B)•••O(2B) interactions with a length of 2.5137(22) Å and an angle of 172°. These values are close to those described in the literature for similar complexes. These interactions provide R22(8) type arrangements, as shown in Fig. 4B obtained using the Diamond Crystal and Molecular Structure 3.2 program [46,47].

3.3. *Theorical spectroscopy and energy transfer process calculations*

The effect of including dispersion models and the solvent effect on the geometry optimization was evaluated using the Root Mean Square Deviation (RMSD). RMSD is the square root of the mean square error between superimposed three-dimensional structures in the same coordinate system. The RMSD values for the optimized structures with the experimental structure as the reference (**Table S3**). The RMSD of the coordination polyhedral of the two complexes was also obtained to analyze the methods.

A plausible explanation for the improved structural description (lower RMSD), when the solvent effect was included in the calculations, is that the various hydrogen bonding interactions are intensified by the solvent effect, leading to an optimized structure that is more in

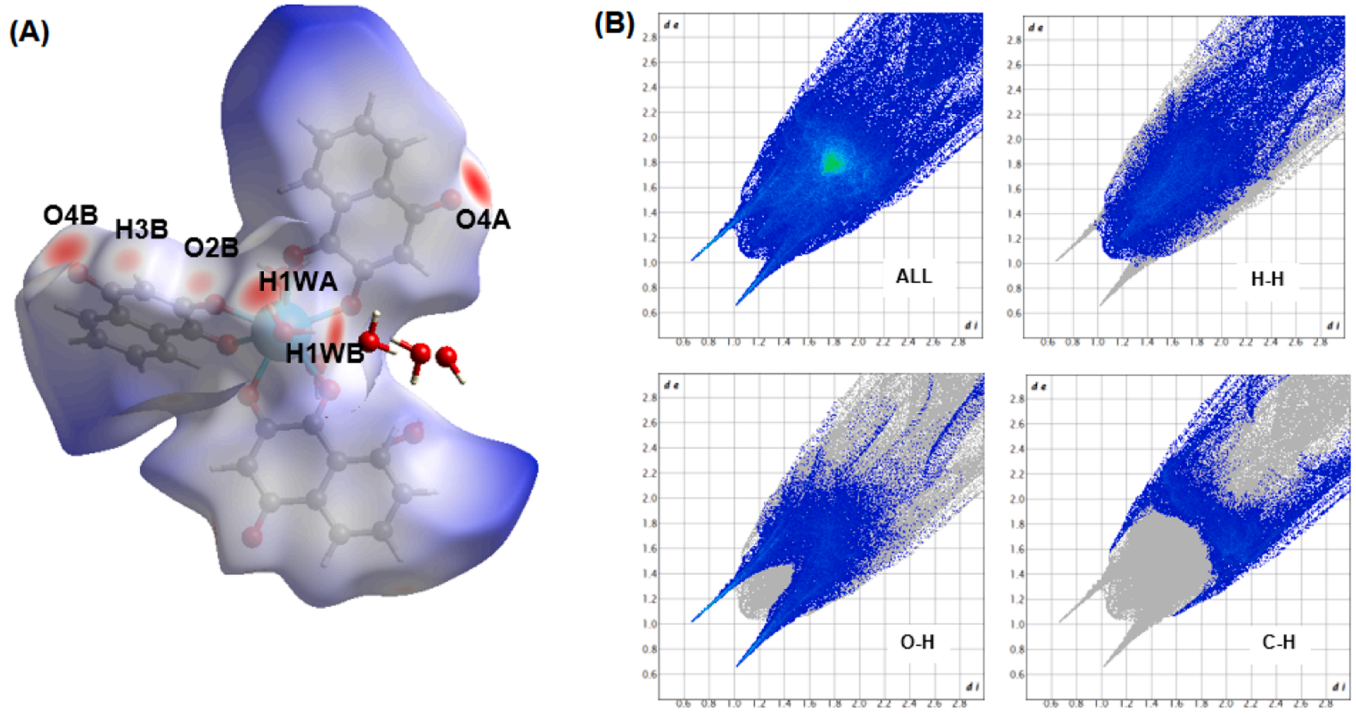

Fig. 3. Hirshfeld surface (A) and view of the *dnorm* mapped (B) of the complex 2.

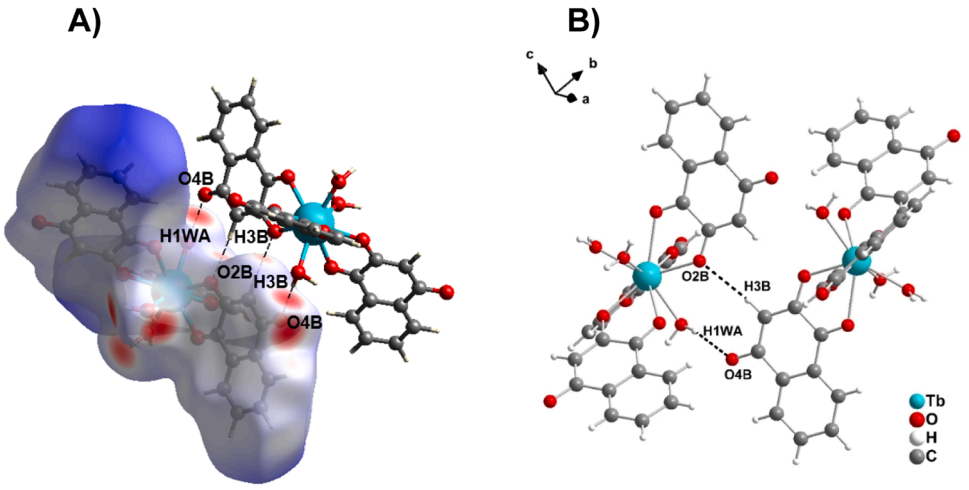

Fig. 4. (A) View of the *dnorm* mapped on the Hirshfeld surface of the 2 representing the molecular interactions. (B) Representation of the $^{R22}(8)$ arrangement along the crystallographic axis *a* formed by the interactions O(1W)-H(1WA)•••O(4B) and C(3B) - H(3B)•••O(2B), symmetry code: (2-x, 1-y, 1-z).

agreement with the experimental one. Table S4 shows that considering the D3 and D4 dispersion models in the structural optimization calculation did not lead to an improvement in the geometric description. Therefore, the geometries calculated (with the PBE1PBE/TZVP/(MWB52 or MWB54)/CPCM level of theory) were considered in the calculation of the excited states of the ligands (**Fig. S5**). Using the Shape program [48] and the coordination polyhedron of each optimized structure obtained with the DFT method, the coordination polyhedron of both structures is best described as a spherical capped square antiprism, which in its ideal form has point group C_{4V}.

Experimental and theoretical absorption spectra of the complexes **1** and **2** are presented in Fig. 5. It can be observed that the TD-DFT method provided theoretical absorption spectra in good agreement with the experimental ones. Due to the close resemblance between the complexes, their respective spectra also exhibit significant similarity. In previous studies, it has been observed that TD-DFT calculations employing the hybrid functional CAM-B3LYP tend to overestimate singlet energy values [25,49,50]. Despite the overestimation of singlet energy values, the TD-DFT method exhibited excellent accuracy for the most intense bands in the low-wavelength region, except for the visible absorption band. The implicit solvent consideration in the TD-DFT calculations redshifted the wavelengths of all bands in the spectrum and enhanced the similarity between the spectra of the two complexes. Additional calculations were performed using the same levels of theory in conjunction with D3 and D4 dispersion effects, but no significant changes were observed in the spectral features of either complex. To further assess the computational results, excited state calculations were also performed using the hybrid functional PBE1PBE for comparison. The PBE1PBE calculations produced a similar absorption spectrum profile to that obtained with the CAM-B3LYP functional, except for a

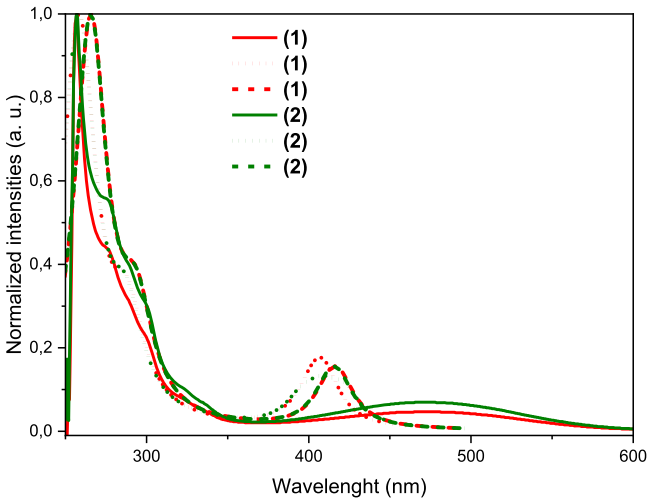

Fig. 5. Theoretical and experimental absorption spectra of 1 and 2 complexes: A TD-DFT approach with CAM-B3LYP/TZVP/MWB52 for 1 and CAM-B3LYP/TZVP/MWB54 for 2.

redshift of all bands by approximately 50–60 nm. Therefore, the CAM-B3LYP results with implicit solvent effects were chosen to interpret spectroscopic properties and model the ligand-metal energy transfer.

To elucidate the nature of the most prominent absorption bands in the UV/Vis region, the electronic transitions responsible for absorption at wavelengths of 265.4 nm and 420.4 nm for complex **1** and 265.2 nm and 419.8 nm for complex **2** were analyzed. **Table S4** summarizes the most critical electronic transitions for characterizing these states. Notably, there is a remarkable similarity in the transitions related to the orbitals with the highest contributions, oscillator strengths, and wavelengths for the two complexes. These similarities are to be expected, as the structures of the complexes are alike, and the Eu^{3+} and Tb^{3+} ions do not directly participate in the energy absorption process.

A graphical representation of the molecular orbitals listed in **Table S4** is provided in **Fig S6**. The homologous orbitals for both complexes exhibit a clear resemblance. The LUMO, LUMO+1, and LUMO+2 orbitals exhibit significant π character in all cases. The HOMO and HOMO-2 orbitals display a remarkable resemblance for both complexes and feature more pronounced *n* electron density regions. These observations enable the characterization of the transitions observed in the visible spectrum as predominantly $n \rightarrow \pi^*$ and $\pi \rightarrow \pi^*$ transitions. In contrast, the HOMO-16, HOMO-10, and HOMO-9 orbitals exhibit a more prominent π character in their compositions, suggesting a $\pi \rightarrow \pi^*$ transition nature for the UV absorption bands. In particular, only the LAW ligands participate in the absorption process for both complexes.

3.4. Energy transfer process

A purely theoretical study of ligand-metal energy transfer was performed to better understand the low emission of the complexes. The complexes showed low emissions in the experimental analyses. It was observed that the expected bands for the transitions related to the coordinated metals, especially the hypersensitive transitions of the type $^5D_0$-$^7F_2$ (~612nm) for Eu(III) (Fig. 6A and 6B) and $^4D_4$-$^7F_5$ (~550 nm) for Tb(III) (**Fig. S7**) are completely lost or displaced.

The energies of the singlet (S) and triplet (T) excited states calculated by TD-DFT are listed in **Table S5**. To model the energy transfer, different channels involving ligand and Ln^{3+} ion levels were investigated. In addition to T1, 24 lower-energy triplets were considered, and their rates were summed for the acceptor levels of the lanthanide ions (Fig. 7). The lowest energy singlet (S1) and the most intense singlet (Sn) were also included. **Table S6** lists the forward (WET) and backward (WBT) energy transfer rates for the singlet and triplet levels of each complex to the acceptor levels of the Eu^{3+} and Tb^{3+} ions. The $^5D_0$ level of Eu^{3+} and the $^5D_4$ level of Tb^{3+} were treated separately because they are the emitting levels.

The most efficient channels for the lowest energy excited states (**Tables S5** and **S6**) are $S_1 \rightarrow {}^5D_0$ for Eu^{3+} and $S_1 \rightarrow {}^5D_4$ for Tb^{3+}, as they have high WET relative to WBT. In contrast, channels involving T_1 are less efficient because T_1 is below the acceptor levels, resulting in WBT > WET. The Sn state, whose energy is significantly higher than the emitter levels, shows minimal interaction, resulting in low WET and WBT values. The other 24 triplet states behave similarly to T_1, with WET < WBT, since T_1 is nearly degenerate with T_2 and T_3 in both complexes. Higher energy triplets contribute less to WET and WBT. The lowest energy ligand states, especially T_1, play a key role in energy transfer due to their population via intraligand decay. However, as shown in **Table S6**, backward rates dominate the T_1-related channels, resulting in a high T_1 population but a low acceptor level population, as shown in Fig. 7. In addition, water molecules coordinated to the metal center contribute to high non-radiative decay rates in Ln^{3+} systems due to O-H vibrational quenching [51].

3.5. Stability studies

Since the experiments required prior solubilization of the complexes in DMSO, we first evaluated the stability of complexes **1** and **2** in this solvent. The results showed that both complexes remain highly stable in DMSO for up to 48 hours (**Fig. S8** and **S9**). Subsequently, we evaluated their stability in a culture medium, and since no significant spectral changes were observed, complexes **1** and **2** were also considered stable in this environment for up to 48 hours (**Figs. S10** and **S11**).

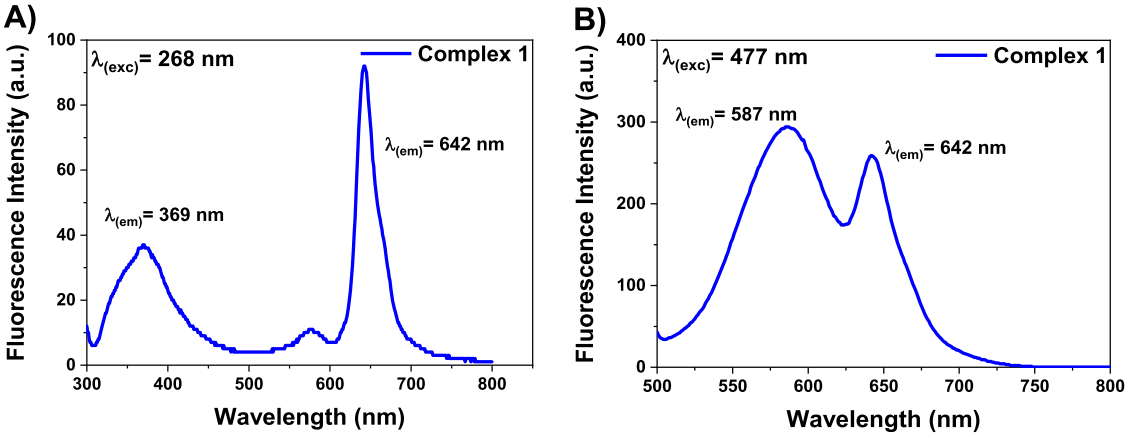

Fig. 6. Emission spectra for complex 1 with excitation in 260 (A) and 477 nm (B). Solvent: DMSO and concentration $1.0x10^{-5}$ M.

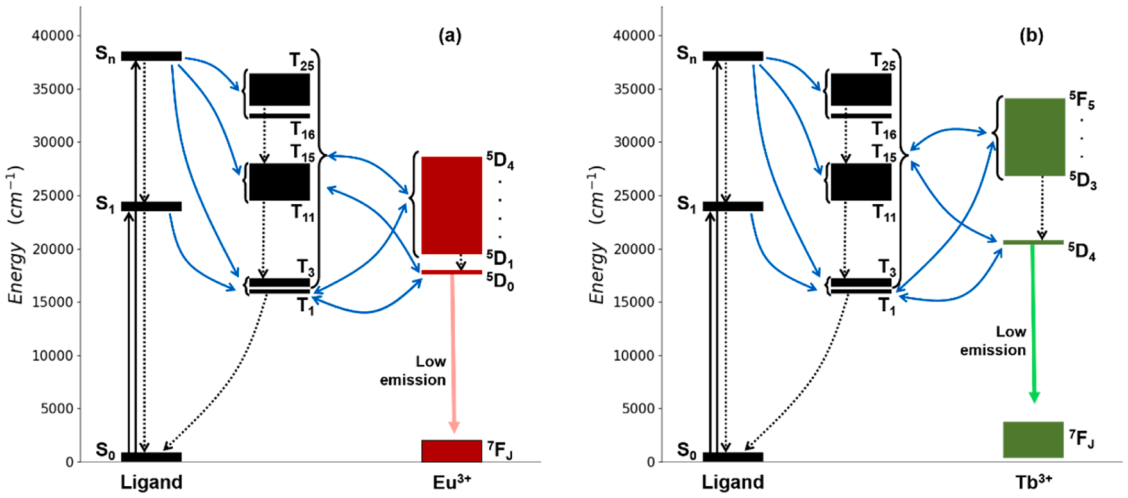

Fig. 7. Diagram of the proposed energy levels describing the energy transfer process in the a) (1) and b) (2) complexes.

3.6. HSA interaction and docking studies

Albumin, a highly abundant blood protein, plays a crucial role as a natural carrier for various molecules, enhancing the pharmacokinetic profiles of numerous drugs and potential antitumor agents [52]. As complex concentrations increase, protein-complex interactions can be monitored by observing fluorescence quenching (Fig. 8). As shown in **Table S7**, the Stern-Volmer constant for both complexes decrease with increasing temperature, particularly for the europium complex, suggesting temperature-dependent binding. The biomolecular quenching rate constant (K_q) is on the order of 10^{13} L mol^{-1} s^{-1}, which exceeds the threshold for dynamic quenching (2.0×10^{10} L mol^{-1} s^{-1}), indicating a static quenching mechanism in HSA-complex formation [32,53,54]. The europium complex shows a moderate binding constant (K_b = 3,25x10^5 at 310K) with albumin. In contrast, complex **2** exhibits strong binding with K_b values around 10^6, potentially limiting its plasma availability but promoting higher uptake by tumor cells. Compared with approved drugs, BI-2536 ($K_b = 3.78 \times 10^6$), warfarin ($K_b = 6.17 \times 10^4$), tenofovir ($K_b = 5.70 \times 10^4$), dexamethasone ($K_b = 7.1 \times 10^3$), and furosemide ($K_b = 1.99 \times 10^5$) the complexes fall within an intermediate binding range, suggesting they may be effectively transported by HSA to tumor cells and subsequently released there [52,54].

It is essential to select an effective scoring function for molecular docking studies to determine the optimal docking positions for the new metal complexes. In this research, the selection of the scoring function was based on the difference between the RMSD values of the highest-ranked re-docking pose of WAR and the pose with the lowest RMSD. For the re-docking of WAR in the B repeat unit of the crystal structure, ChemScore was the scoring function that produced the best results. Moreover, the tautomeric state of the HIS242 residue within HSA that exhibited the lowest RMSD was identified as the NE2 state, as indicated in **Table S8**.

The binding site was delineated in a manner analogous to the crystallized WAR ligand within Sudlow site I. The quality of the redocking procedure was evaluated based on the root mean square deviation (RMSD) of the highest-ranked pose, which served as the criterion for assessing the computational routine's capability to reproduce the original positioning of the WAR ligand within the crystal structure (Fig. 9). According to established literature, redocking validations that yield an RMSD of less than 2 Å are regarded as adequate for this assessment. In the present study, an RMSD of 0.6962 Å between heavy atoms was achieved, thereby confirming the reliability of the employed methodology.

Upon analyzing the docking results, both compounds demonstrated stable conformations within the Sudlow I site. Due to their more ionic character in comparison to WAR, they established polar contacts, including classical N–H···O and non-classical C–H···π hydrogen bonds with residues situated in a more external region of the binding pocket than the co-ligand (Fig. 10). Furthermore, this behavior may be

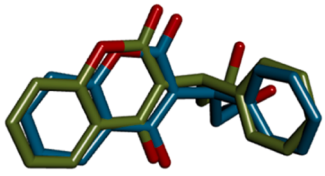

Fig. 9. The redocked WAR, shown in blue with a lower RMSD, is superimposed with the experimentally determined WAR from X-ray diffraction, represented in green, co-crystallized in the Sudlow site I.

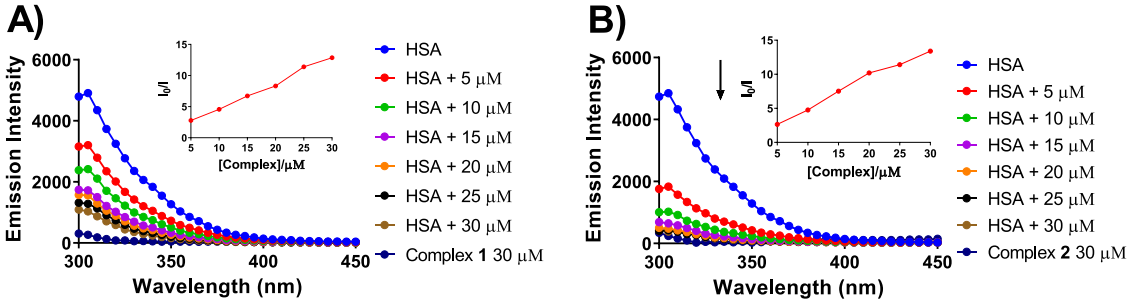

Fig. 8. Fluorescence spectrum for HSA (1.0 x 10−5M) in the presence of increasing amounts of the complex 2 (A) and complex 2 (B) (from 5 – 30μM) at 298K, λ_{ex} =280 nm and λ_{em} = 330 nm. Plot of I_0/I vs [Complex/HSA] at 298K.

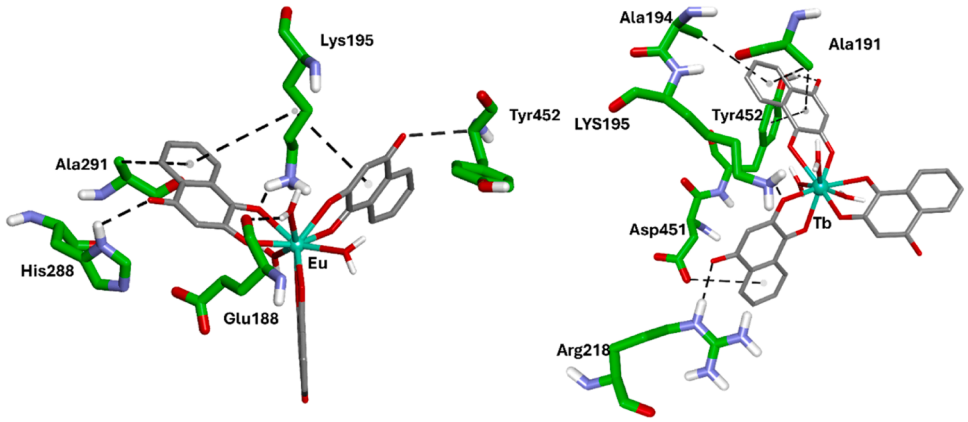

Fig. 10. Illustrates the best docking conformations for Eu(III) and Tb(III) complexes within Sudlow site I of the HSA protein. Predominantly, H-bonding interactions are fundamental to the establishment of connections with key residues located in the hydrophilic subunit of the pocket.

associated with the larger molecular volumes of the complexes when contrasted with the ligand. The calculated ΔG, expressed in kcal mol^{-1}, for WAR and the Eu(III) and Tb(III) complexes were -39.65, -33.70, and -28.72, respectively. These findings indicate that akin to WAR, the metal complexes may be transported by the HSA protein into the bio-phase through interactions with the Sudlow I pocket.

3.7. ct-DNA interaction studies

The identification of biological targets is critical to the development of antitumor agents, and direct testing with biomolecules serves as an essential first step in this process. Biomolecules such as DNA, topoisomerase enzymes, and proteins such as albumin play fundamental roles in cellular functions, including drug delivery to cells via HSA and DNA replication facilitated by type I and II topoisomerase enzymes. Direct interactions with these biomolecules can be assessed using various techniques, fluorescence, viscosity measurements, circular dichroism, and electrophoresis, each of which provides valuable insight into the modes of interaction of compounds with their targets.

UV-Vis spectroscopy is commonly used to assess interactions between biomolecules, such as DNA, and small molecules (e.g., metal complexes), as it can detect conformational changes in DNA bands resulting from electrostatic or intercalative (π) interactions. To highlight these interactions, changes in absorbance are monitored by varying biomolecule concentrations while keeping the metal complex concentration constant [55]. No spectral changes were observed for complex **1** (Fig. 11A), suggesting little to no interaction or only weak electrostatic interaction. In contrast, complex Tb(III) (complex **2**) exhibited a slight hypochromic effect at 450 nm (Fig. 11B), indicating stabilization of the DNA secondary structure by electrostatic interactions. The binding constant (K_b) calculated via the Benesi-Hildebrand equation is 1.53 x 10^5, suggesting a moderate to strong electrostatic interaction with DNA bases [56].

For further investigation of the interaction type, we used circular dichroism (CD) spectroscopy, which provides a sensitive analysis of the double helix conformation of DNA. B-DNA, the most common form of DNA, shows two characteristic CD bands: a positive band at 277 nm due to base stacking and a negative band at 243 nm associated with the helicity of the double strands (Fig. 12). Upon addition of increasing concentrations of complexes **1** and **2**, significant changes in the CD spectrum were observed (Fig. 12A and 12B), with a reduction in both band intensities, indicating strong interactions with the DNA double helix [56,57]. Similar effects have been reported for other metal-based compounds [58]. Structurally, this suggests possible covalent bonding with phosphate groups or nitrogenous bases. In addition, the affinity of these metals for oxoanions, such as phosphates, and the planarity of the lawsone ligands, which may facilitate π-stacking with nitrogenous bases, also support potential intercalative interactions [59].

Viscosity experiments were performed to determine whether the interaction of the metal complexes with DNA was by intercalation or covalent binding. Thiazole orange and cisplatin were also used as positive controls for intercalative and covalent modes, respectively (Fig. 13). Their effects on DNA viscosity can distinguish intercalation and covalent binding. Intercalation increases viscosity by lengthening the DNA strand, while covalent binding decreases viscosity due to significant twisting and bending of the double helix [37]. As observed in

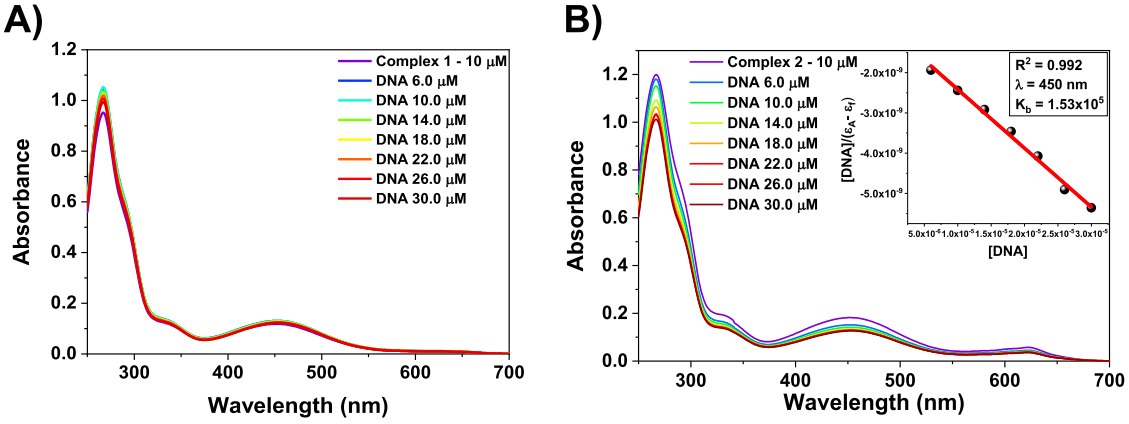

Fig. 11. Spectrophotometric titration spectra for complexes 1 (A) and complex 2 (B) in concentration of 10 μM, with increased concentration of ct-DNA (0-30 μM) and K_b constant was calculated at λ = 450 nm.

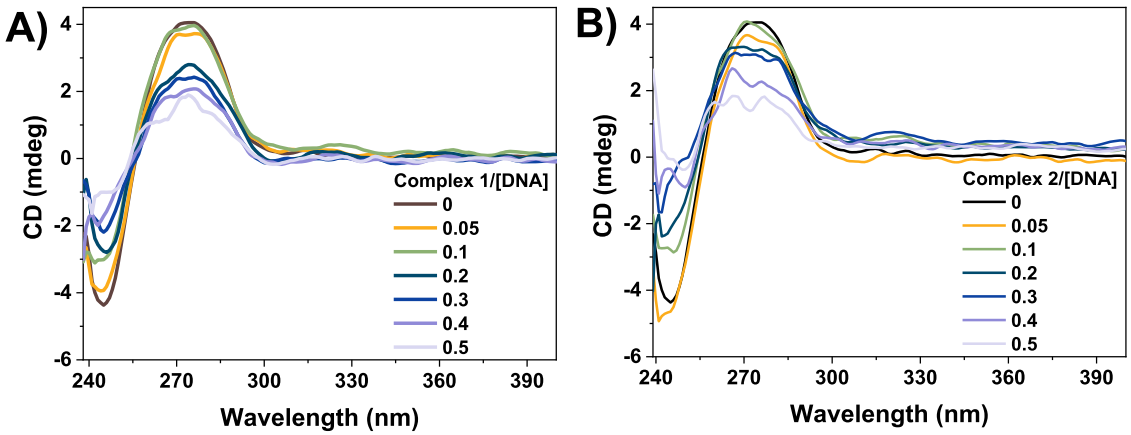

Fig. 12. CD spectra of ct-DNA (100 μM) in the absence and presence of complex 2 at different molar ratios [complex]/[DNA] (0.00–0.50) at 298 K in a Tris-HCl buffer containing 20 % DMSO.

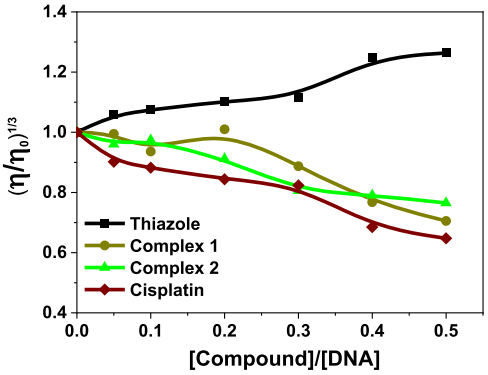

Fig. 13. Viscosity of ct-DNA (100 μM) in presence of (1) and complex 2 (20–200 μM) and thiazole orange and cisplatin references, at different molar ratios [compound]/[DNA] (0.05, 0.1, 0.2, 0.3, 0.4 and 0.5) containing 20 % DMSO.

Fig. 13, complexes **1** and **2** present a similar behavior to cisplatin, causing a decrease in relative viscosity, indicating that both can interact through covalent bonds with the biomolecule. These results are consistent with those observed in CD experiments.

Fluorescence competition assays were performed using Hoechst 33258 and Thiazole Orange, which bind to DNA through distinct mechanisms. Hoechst 33258 interacts via minor groove binding, while Thiazole Orange intercalates between base pairs. Both dyes emit fluorescence when excited at specific wavelengths [38,60]. Displacement of these dyes from DNA by an external agent can indicate conformational changes in DNA structure. Assays with complexes **1** and **2** at various concentrations (Fig. 14, **S15**, and **S16**) showed similar fluorescence decay behavior, with dye displacement exceeding 50 % at the highest complex concentrations. This result suggests that both complexes can interact directly with DNA, potentially causing conformational changes or forming covalent bonds that displace the dyes used in these studies [38].

3.8. *Electrophoretic mobility of the plasmid pBR322 and top IIα and IB inhibition assay in Gel agarose*

Agarose gel electrophoresis was employed to investigate the interacting/cleaving properties of complexes **1** and **2**. The plasmid DNA can take on different forms, each of which migrates in the gel, depending on its size and shape (i) Supercoiled form (SC) is the most compact and migrates faster through the gel; (ii) open circular form (OC) resulted from a single break on DNA and present lower migration rates; (L) linear form is a resulted from double break strands and migrates between supercoiled and circular forms. The effect of complexes **1** and **2** are presented in Fig. 15.

The complexes exhibit interactions at high concentrations of 100 μM ([L1: (1) and L4: (2)]. At this concentration, the spectroscopic data indicates that the formation of covalent bonds with DNA impedes plasmid mobility, resulting in a more pronounced presence of the open circle (OC) form. In contrast, cisplatin induces DNA cleavage through covalent bonding at much lower concentrations, beginning at just 5 μM (C+) [36] (Fig. 15).

The electrophoresis technique is essential for studying the activity of topoisomerase enzymes, which can cleave plasmid and prevent it from migrating through an agarose gel. Topoisomerases play an essential role in maintaining the stability of the human genome by managing DNA topology. They are classified into two major families, Type I and Type II, which include subfamilies such as Topo Iβ and Topo IIα. During the cell

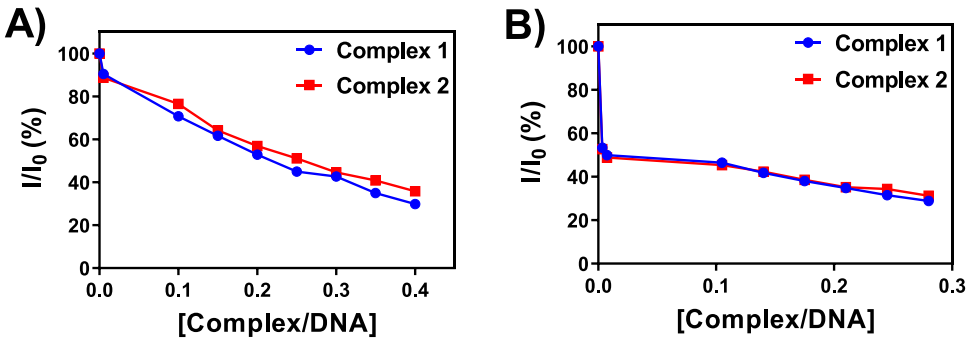

Fig. 14. Plot of I/I_0 (%) versus [complex/DNA+Hoeschst] (A) and [complex/DNA+Thiazole orange] (B) for complexes 1 and 2.

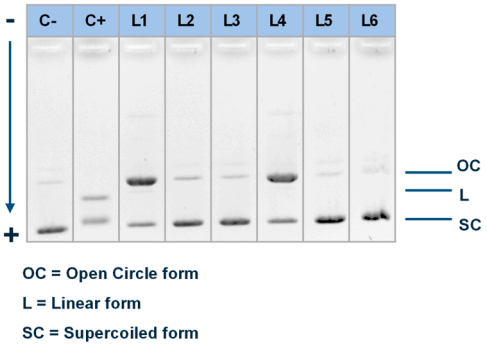

Fig. 15. Electrophoresis mobility shift assay of the plasmid pBR322 with; Negative control: DNA+DMSO; Positive control: Cisplatin (5μM) + DNA; L1: (1) 100μM + DNA; L2: (1) 10μM + DNA; L3: (1) 1μM + DNA. L4: (2) 100μM + DNA; L5: (2) 10μM + DNA; L6: (2) 1μM + DNA.

cycle, these enzymes induce breaks in DNA - Topo Iβ creates single-strand breaks, while Topo IIα creates double-strand breaks. Depending on the interactions between the topoisomerases and the complexes, these transient breaks can lead to permanent breaks, potentially resulting in cell death. This makes these enzymes critical therapeutic targets [61].

Interaction assays with TOPO IIα and Iβ (Figs. 16 and **S17**) show different behaviors. The compounds effectively inhibit TOPO IIα (L1 and L4) at a concentration of 50 μM but show no activity against Iβ. Both subfamilies play critical roles in cell replication and are often overexpressed in tumor cells [61]. Notably, at the same concentration as plasmid pBR233 alone (L8 and L9 in **Fig. S17**), the compounds do not interact with the plasmid, indicating selectivity for the enzyme. One hypothesis based on the preference for TOPO IIα is that the complexes may interfere with the catalytic cycle of this enzyme, possibly stabilizing the formation of TOPO complexes and preventing ATP (adenosine triphosphate) from binding to the ATPase site.

4. Conclusions

Two complexes, Eu-Lawsone and Tb-Lawsone, were synthesized and characterized using single crystal X-ray, CHN analysis, molar conductivity, voltammetry, magnetic susceptibility, IR spectroscopy, fluorescence and UV-Vis spectroscopy. UV-Vis data agreed with theoretical predictions, while emission spectroscopy revealed a significant energy gap between ligand and metal excited states, contributing to lower emissions. Both complexes interact significantly with DNA, as supported by UV-Vis titration, circular dichroism, viscosity measurements, and dye shift assays. Conformational changes in DNA were confirmed by electrophoresis, which revealed circular DNA structures at 100 μM.

Notably, both complexes effectively inhibited TOPO IIα at 50 μM, an important target in cancer therapy. The Eu complex showed potential as a drug carrier by binding to human serum albumin (HSA), enabling targeted drug delivery. In contrast, the high HSA binding constant of the Tb complex ($K_b = 1.29 \times 10^6$ at 310 K) suggests challenges in biodistribution due to stable HSA-complex adduct formation. These findings highlight the potential of these complexes as targeted anticancer agents, with future studies aimed at optimizing their design for enhanced biomolecular interactions.

CRediT authorship contribution statement

Josias S. Rocha: Writing – review & editing, Writing – original draft, Project administration, Methodology, Formal analysis, Data curation, Conceptualization. **George B.S. Pereira:** Visualization, Methodology, Formal analysis, Data curation, Conceptualization. **Marcos V. Palmeira-Mello:** Visualization, Methodology, Investigation, Formal analysis, Data curation. **Willyan F. Oliveira:** Writing – review & editing,

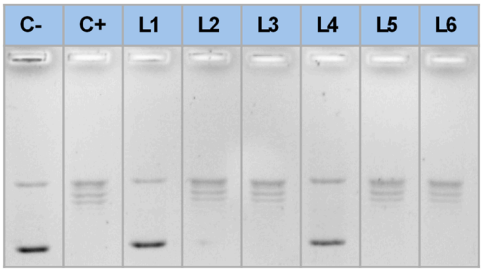

Fig. 16. Electrophoresis mobility shift assay of the plasmid pBR322 relaxed by a human TOPO IIα by agarose gel electrophoresis in 1 % agarose gel. C-: DMSO + MIX (pBR233+ATP+Buffer assay); C+: MIX + TOPO IIα + DMSO; L1: (1) 50μM + MIX + TOPO IIα; L2 (1) 10μM + MIX + TOPO IIα; L3 (1) 1μM + MIX + TOPO IIα; L4 (2) 50μM + MIX + TOPO IIα; L5 (2) 10μM + MIX + TOPO IIα; L6 (2) 1μM + MIX + TOPO IIα.

Software, Methodology, Formal analysis, Data curation. **Jocely L. Dutra:** Visualization, Methodology, Formal analysis, Data curation. **Tamara Teixeira:** Visualization, Methodology, Formal analysis, Data curation. **Nádija N.P. da Silva:** Validation, Methodology, Formal analysis, Data curation. **Gabriela P. Oliveira:** Methodology, Formal analysis, Data curation. **Paulo C. Gomes-Junior:** Methodology, Formal analysis, Data curation. **Anna C.S.J. Passaes:** Formal analysis, Methodology. **João H. Araujo-Neto:** Validation, Software, Investigation, Formal analysis, Data curation. **Alzir A. Batista:** Supervision, Resources, Project administration, Funding acquisition. **Javier Ellena:** Resources, Methodology, Funding acquisition, Formal analysis. **José D. L. Dutra:** Visualization, Resources, Methodology, Investigation, Data curation. **Renan L. Farias:** Formal analysis, Methodology, Software. **Fillipe V. Rocha:** Writing – review & editing, Visualization, Project administration, Methodology, Funding acquisition.

Declaration of competing interest

The authors declare that they have no known competing financial interests or personal relationships that could have appeared to influence the work reported in this paper.

Acknowledgments

We thank CNPq (401681/2023-8) for financial support. M.V.P.-M. thanks the São Paulo State Research Support Foundation (FAPESP, process 2021/01787-0). F.V.R. thanks the São Paulo State Research Support Foundation (FAPESP, process 2022/02876-0), FINEP (01.22.0181) and (CAPES code 001). WFO appreciate the financial support from the Brazilian funding agency CAPES.

Supplementary materials

Supplementary material associated with this article can be found, in the online version, at doi:10.1016/j.molstruc.2025.141790.

Data availability

Data will be made available on request.

References

[1] T. Lazarević, A. Rilak, Ž.D. Bugarčić, Platinum, palladium, gold and ruthenium complexes as anticancer agents: current clinical uses, cytotoxicity studies and future perspectives, Eur. J. Med. Chem. 142 (2017) 8–31, https://doi.org/10.1016/j.ejmech.2017.04.007.
[2] T. Xian, Q. Meng, F. Gao, M. Hu, X. Wang, Functionalization of luminescent lanthanide complexes for biomedical applications, Coord. Chem. Rev. 474 (2023) 214866, https://doi.org/10.1016/j.ccr.2022.214866.
[3] G. Bao, Lanthanide complexes for drug delivery and therapeutics, J. Lumin. 228 (2020) 117622, https://doi.org/10.1016/j.jlumin.2020.117622.

[4] E. Mathieu, A. Sipos, E. Demeyere, D. Phipps, D. Sakaveli, K.E. Borbas, Lanthanide-based tools for the investigation of cellular environments, Chem. Commun. 54 (2018) 10021–10035, https://doi.org/10.1039/C8CC05271A.

[5] T.S. Martins, P.C. Isolani, Terras raras: Aplicações industriais e biológicas, Quim. Nova 28 (2005) 111–117, https://doi.org/10.1590/S0100-40422005000100020.

[6] M. Wang, Y. Kitagawa, Y. Hasegawa, Current development of lanthanide complexes for biomedical applications, Chem. Asian J. 19 (2024) e202400038, https://doi.org/10.1002/asia.202400038.

[7] H.K. Swedan, A.E. Kassab, E.M. Gedawy, S.E. Elmeligie, Topoisomerase II inhibitors design: early studies and new perspectives, Bioorg. Chem. 136 (2023) 106548, https://doi.org/10.1016/j.bioorg.2023.106548.

[8] S. Oramas-Royo, C. Torrejón, I. Cuadrado, R. Hernández-Molina, S. Hortelano, A. Estévez-Braun, B. De Las Heras, Synthesis and cytotoxic activity of metallic complexes of lawsone, Bioorg. Med. Chem. 21 (2013) 2471–2477, https://doi.org/10.1016/j.bmc.2013.03.002.

[9] F.V.C. Kock, A.R. Costa, K.M. de Oliveira, A.A. Batista, A.G. Ferreira, T. Venâncio, A supramolecular interaction of a ruthenium complex with calf-thymus DNA: a ligand binding approach by NMR spectroscopy, Front. Chem. 7 (2019) 1–10, https://doi.org/10.3389/fchem.2019.00762.

[10] K.M. Oliveira, E.J. Peterson, M.C. Carroccia, M.R. Cominetti, V.M. Deflon, N. P. Farrell, A.A. Batista, R.S. Correa, Ru(ii)-Naphthoquinone complexes with high selectivity for triple-negative breast cancer, Dalton Trans. 49 (2020) 16193–16203, https://doi.org/10.1039/d0dt01091j.

[11] M.V.P. de Mello, G. Cebrián-Torrejón, J.R. Pereira, C. dos Santos Moreira, C.B. de S.M.R. Gomes, D.R. da Rocha, E.M. de Souza Fagundes, G.B. Ferreira, M. Lanznaster, Evaluation of 5-hydroxy-1,4-naphthoquinone-cobalt(III) complexes for hypoxia-activated drug delivery, J. Inorg. Biochem. 199 (2019) 110756, https://doi.org/10.1016/j.jinorgbio.2019.110756.

[12] Z.F. Chen, X.Y. Song, Y. Peng, X. Hong, Y.C. Liu, H. Liang, High cytotoxicity of dihalo-substituted 8-quinolinolato-lanthanides, Dalton Trans. 40 (2011) 1684–1692, https://doi.org/10.1039/c0dt01310b.

[13] J.H. Wei, Z.F. Chen, J.L. Qin, Y.C. Liu, Z.Q. Li, T.M. Khan, M. Wang, Y.H. Jiang, W. Y. Shen, H. Liang, Water-soluble oxoglaucine-Y(iii), Dy(iii) complexes: in vitro and in vivo anticancer activities by triggering DNA damage, leading to S phase arrest and apoptosis, Dalton Trans. 44 (2015) 11408–11419, https://doi.org/10.1039/c5dt00926j.

[14] F. Bisceglie, A. Musiari, S. Pinelli, R. Alinovi, I. Menozzi, E. Polverini, P. Tarasconi, M. Tavone, G. Pelosi, Quinoline-2-carboxaldehyde thiosemicarbazones and their Cu(II) and Ni(II) complexes as topoisomerase IIa inhibitors, J. Inorg. Biochem. 152 (2015) 10–19, https://doi.org/10.1016/j.jinorgbio.2015.08.008.

[15] G.M. Sheldrick, A short history of SHELX, Acta Crystallogr. Sect. A Found. Crystallogr. 64 (2008) 112–122, https://doi.org/10.1107/S0108767307043930.

[16] C.F. MacRae, I. Sovago, S.J. Cottrell, P.T.A. Galek, P. McCabe, E. Pidcock, M. Platings, G.P. Shields, J.S. Stevens, M. Towler, P.A. Wood, Mercury 4.0: from visualization to analysis, design and prediction, J. Appl. Crystallogr. 53 (2020) 226–235, https://doi.org/10.1107/S1600576719014092.

[17] P. Van Der Sluis, A.L. Spek, BYPASS: an effective method for the refinement of crystal structures containing disordered solvent regions, Acta Crystallogr. Sect. A 46 (1990) 194–201, https://doi.org/10.1107/S0108767389011189.

[18] F. Neese, Software update: the ORCA program system—Version 5.0, Wiley Interdiscip, Rev. Comput. Mol. Sci. 12 (2022), https://doi.org/10.1002/wcms.1606.

[19] E. Caldeweyher, C. Bannwarth, S. Grimme, Extension of the D3 dispersion coefficient model, J. Chem. Phys. (2017) 147, https://doi.org/10.1063/1.4993215.

[20] M. Cossi, N. Rega, G. Scalmani, V. Barone, Energies, structures, and electronic properties of molecules in solution with the C-PCM solvation model, J. Comput. Chem. 24 (2003) 669–681, https://doi.org/10.1002/jcc.10189.

[21] O.L. Malta, Ligand - rare-earth ion energy transfer in coordination compounds. A theoretical approach, J. Lumin. 71 (1997) 229–236, https://doi.org/10.1016/S0022-2313(96)00126-3.

[22] F.R.G.E. Silva, O.L. Malta, Calculation of the ligand-lanthanide ion energy transfer rate in coordination compounds: contributions of exchange interactions, J. Alloys. Compd. 250 (1997) 427–430, https://doi.org/10.1016/s0925-8388(96)02563-7.

[23] J.D.L. Dutra, T.D. Bispo, R.O. Freire, LUMPAC lanthanide luminescence software: efficient and user friendly, J. Comput. Chem. 35 (2014) 772–775, https://doi.org/10.1002/jcc.23542.

[24] R. Ilmi, X. Xia, J.D.L. Dutra, G.S. Santos, L. Zhou, W.Y. Wong, P.R. Raithby, M. S. Khan, Highly efficient red-emitting OLEDs prepared from nona-coordinated europium(III) complexes, ACS Appl. Electron. Mater. 6 (2024) 2624–2638, https://doi.org/10.1021/acsaelm.4c00208.

[25] R. Ilmi, J. Wang, J.D.L. Dutra, L. Zhou, W.Y. Wong, P.R. Raithby, M.S. Khan, Efficient red organic light emitting diodes of nona coordinate europium Tris (β-Diketonato) complexes bearing 4′-Phenyl-2,2′:6′,2″-terpyridine, Chem. A Eur. J. 29 (2023), https://doi.org/10.1002/chem.202300376.

[26] I.J. Al-Busaidi, R. Ilmi, D. Zhang, J.D.L. Dutra, W.F. Oliveira, N.K. Al Rasbi, L. Zhou, W.Y. Wong, P.R. Raithby, M.S. Khan, Synthesis and photophysical properties of ternary β-diketonate europium(III) complexes incorporating bipyridine and its derivatives, Dye Pigment (2022) 197, https://doi.org/10.1016/j.dyepig.2021.109879.

[27] I.J. Al-Busaidi, R. Ilmi, J.D.L. Dutra, W.F. Oliveira, A. Haque, N.K. Al Rasbi, F. Marken, P.R. Raithby, M.S. Khan, Utilization of a Pt(ii) di-yne chromophore incorporating a 2,2′-bipyridine-5,5′-diyl spacer as a chelate to synthesize a green and red emitting d-f-d heterotrinuclear complex, Dalton Trans. 50 (2021) 1465–1477, https://doi.org/10.1039/d0dt04198j.

[28] A.S. Borges, J.D.L. Dutra, G.S. Santos, R. Diniz, J. Kai, M.H. Araujo, Theoretical and experimental spectroscopic investigation of new Eu(III)-FOD complex containing 2-pyrrolidone ligand, J. Mol. Model. (2021) 27, https://doi.org/10.1007/s00894-021-04883-1.

[29] A.R.B.S. Galaço, L.T. Jesus, R.O. Freire, M. De Oliveira, O.A. Serra, Experimental and theoretical studies of glyphosate detection in water by an europium luminescent complex and effective adsorption by HKUST-1 and IRMOF-3, J. Agric. Food Chem. 68 (2020) 9664–9672, https://doi.org/10.1021/acs.jafc.0c03574.

[30] M.S. Khan, R. Ilmi, W. Sun, J.D.L. Dutra, W.F. Oliveira, L. Zhou, W.Y. Wong, P. R. Raithby, Bright and efficient red emitting electroluminescent devices fabricated from ternary europium complexes, J. Mater. Chem. C 8 (2020) 5600–5612, https://doi.org/10.1039/d0tc00749h.

[31] B. Francis, M.M. Nolasco, P. Brandão, R.A.S. Ferreira, R.S. Carvalho, M. Cremona, L.D. Carlos, Efficient visible-light-excitable Eu3+ complexes for red organic light-emitting diodes, Eur. J. Inorg. Chem. (2020) 1260–1270, https://doi.org/10.1002/ejic.202000027, 2020.

[32] J. Ghuman, P.A. Zunszain, I. Petitpas, A.A. Bhattacharya, M. Otagiri, S. Curry, Structural basis of the drug-binding specificity of human serum albumin, J. Mol. Biol. 353 (2005) 38–52, https://doi.org/10.1016/j.jmb.2005.07.075.

[33] M.U. Johansson, V. Zoete, O. Michielin, N. Guex, Defining and searching for structural motifs using DeepView/Swiss-PdbViewer, BMC Bioinform. 13 (2012), https://doi.org/10.1186/1471-2105-13-173.

[34] Y.C. Chen, Erratum: beware of docking! (Trends in Pharmacological Sciences (2015) 36:9), Trends Pharmacol. Sci. 36 (2015) 617, https://doi.org/10.1016/j.tips.2015.01.004.

[35] H. Kemmish, M. Fasnacht, L. Yan, Fully automated antibody structure prediction using BIOVIA tools: validation study, PLoS One 12 (2017) 1–26, https://doi.org/10.1371/journal.pone.0177923.

[36] J.S. Rocha, G.B.S. Pereira, G.P. Oliveira, M.A. Lima, J.H. Araujo-Neto, L.S. Pinto, M.R. Forim, R.D. Zanetti, A.V.G. Netto, E.E. Castellano, F.V. Rocha, Synthesis and characterization of silver(I) complexes bearing phenanthroline derivatives as ligands: cytotoxicity and DNA interaction evaluation, Inorg. Chem. Commun. (2021) 131, https://doi.org/10.1016/j.inoche.2021.108757.

[37] G.H. Ribeiro, A.A. Batista, A.P.M. Guedes, T.D. de Oliveira, C.R.S.T.B. de Correia, L. Colina-Vegas, M.A. Lima, J.A. Nóbrega, M.R. Cominetti, F.V. Rocha, A. G. Ferreira, E.E. Castellano, F.R. Teixeira, Ruthenium(II) phosphine/mercapto complexes: their in vitro cytotoxicity evaluation and actions as inhibitors of topoisomerase and proteasome acting as possible triggers of cell death induction, Inorg. Chem. 59 (2020) 15004–15018, https://doi.org/10.1021/acs.inorgchem.0c01835.

[38] W. Villarreal, L. Colina-Vegas, G. Visbal, O. Corona, R.S. Corrêa, J. Ellena, M. R. Cominetti, A.A. Batista, M. Navarro, Copper(I)-phosphine polypyridyl complexes: synthesis, characterization, DNA/HSA binding study, and antiproliferative activity, Inorg. Chem. 56 (2017) 3781–3793, https://doi.org/10.1021/acs.inorgchem.6b02419.

[39] M.A. Lima, V.A. Costa, M.A. Franco, G.P. de Oliveira, V.M. Deflon, F.V. Rocha, Palladium(II) complexes bearing thiosemicarbazone and phosphines as inhibitors of DNA-topoisomerase II enzyme: synthesis, characterizations and biological studies, Inorg. Chem. Commun. 112 (2020) 107708, https://doi.org/10.1016/j.inoche.2019.107708.

[40] K. Iftikhar, M. Sayeed, N. Ahmad, Mixed-ligand complexes of trivalent lanthanide ions with β-Diketones and heterocyclic amines, Inorg. Chem. 21 (1982) 80–84, https://doi.org/10.1021/ic00131a015.

[41] Z. Ahmed, K. Iftikhar, Solution studies of lanthanide (III) complexes based on l,l,l,5,5,5-hexafluoro-2,4-pentanedione and 1,10-phenanthroline Part-I: synthesis,1H NMR, 4f-4f absorption and photoluminescence, Inorg. Chim. Acta 363 (2010) 2606–2615, https://doi.org/10.1016/j.ica.2010.04.040.

[42] Z. Ahmed, K. Iftikhar, Synthesis, luminescence and NMR studies of lanthanide (III) complexes with hexafluoroacetylacetone and phenanthroline. Part II, Inorg. Chim. Acta 392 (2012) 165–176, https://doi.org/10.1016/j.ica.2012.06.032.

[43] W.J. Geary, The use of conductivity measurements in organic solvents for the characterisation of coordination compounds, Coord. Chem. Rev. (1971), https://doi.org/10.1016/S0010-8545(00)80009-0.

[44] A.V. Todkary, R. Dalvi, S. Salunke-Gawali, J. Linares, F. Varret, J. Marrot, J. V. Yakhmi, M. Bhadbhade, D. Srinivas, S.P. Gejji, S.Y. Rane, SOM assembly of hydroxynaphthoquinone and its oxime: polymorphic X-ray structures and EPR studies, Spectrochim. Acta A Mol. Biomol. Spectrosc. 63 (2006) 130–138, https://doi.org/10.1016/j.saa.2005.04.054.

[45] A. Gonçalves, M.M. da Cruz, L.O. Biscoli, N.A. Cabeza, J.T. Facco, H.L.B.V. de Barros, E.R. Botero, J.H. de Araujo-Neto, J. Ellena, A.R. Fiorucci, L.C.S. de Oliveira, J.M. Stropa, G.A. Casagrande, L.R.V. Favarin, D.C.M. Rodrigues, A. dos Anjos, X-ray structure, chelation enhanced fluorescence effect, thermal and redox properties of a new europium(III) complex based on bioactive naphthoquinone, Inorg. Chim. Acta (2023) 558, https://doi.org/10.1016/j.ica.2023.121758.

[46] S.S. Batsanov, Van der Waals radii of elements, Inorg. Mater. 37 (2001) 871–885, https://doi.org/10.1023/A:1011625728803.

[47] T.M. Seck, M.N. Gueye, I.E. Thiam, O. Diouf, M. Gaye, P. Retailleau, Synthesis, spectroscopic and X-ray structure determination of a new mononuclear terbium (III) complex from the ligand N,N'-1,5-bis(pyridylmethylidene) carbonohydrazone (H2L), Earthline J. Chem. Sci. 9 (2022) 121–137, https://doi.org/10.34198/ejcs.9123.121137.

[48] M. Pinsky, C. Dryzun, D. Casanova, P. Alemany, D. Avnir, Analytical methods for calculating continuous symmetry measures and the chirality measure, J. Comput. Chem. 29 (2008) 2712–2721, https://doi.org/10.1002/jcc.20990.

[49] R. Ilmi, D. Zhang, J.D.L. Dutra, N. Dege, L. Zhou, W.Y. Wong, P.R. Raithby, M. S. Khan, A tris β-diketonate europium(III) complex based OLED fabricated by

thermal evaporation method displaying efficient bright red emission, Org. Electron. 96 (2021) 106216, https://doi.org/10.1016/j.orgel.2021.106216.
[50] R. Ilmi, W. Sun, J.D.L. Dutra, N.K. Al-Rasbi, L. Zhou, P.C. Qian, W.Y. Wong, P. R. Raithby, M.S. Khan, Monochromatic red electroluminescence from a homodinuclear europium(iii) complex of a β-diketone tethered by 2,2′-bipyrimidine, J. Mater. Chem. C 8 (2020) 9816–9827, https://doi.org/10.1039/d0tc02181d.
[51] A. Døssing, Luminescence from lanthanide(3+) ions in solution, Eur. J. Inorg. Chem. (2005) 1425–1434, https://doi.org/10.1002/ejic.200401043.
[52] J. Fernández-Sainz, P.J. Pacheco-Liñán, J.M. Granadino-Roldán, I. Bravo, A. Garzón, J. Rubio-Martínez, J. Albaladejo, Binding of the anticancer drug BI-2536 to human serum albumin. A spectroscopic and theoretical study, J. Photochem. Photobiol. B Biol. 172 (2017) 77–87, https://doi.org/10.1016/j.jphotobiol.2017.05.016.
[53] A. Hussain, D. Lahiri, M.S. Ameerunisha Begum, S. Saha, R. Majumdar, R.R. Dighe, A.R. Chakravarty, Photocytotoxic Lanthanum(III) and gadolinium(III) complexes of phenanthroline bases showing light-induced DNA cleavage activity, Inorg. Chem. 49 (2010) 4036–4045, https://doi.org/10.1021/ic901791f.
[54] X. Zhao, R. Liu, Z. Chi, Y. Teng, P. Qin, New insights into the behavior of bovine serum albumin adsorbed onto carbon nanotubes: comprehensive spectroscopic studies, J. Phys. Chem. B 114 (2010) 5625–5631, https://doi.org/10.1021/jp100903x.
[55] M. Sirajuddin, S. Ali, A. Badshah, Drug-DNA interactions and their study by UV-Visible, fluorescence spectroscopies and cyclic voltametry, J. Photochem. Photobiol. B Biol. 124 (2013) 1–19, https://doi.org/10.1016/j.jphotobiol.2013.03.013.
[56] S.U. Rehman, T. Sarwar, M.A. Husain, H.M. Ishqi, M. Tabish, Studying non-covalent drug-DNA interactions, Arch. Biochem. Biophys. 576 (2015) 49–60, https://doi.org/10.1016/j.abb.2015.03.024.
[57] J.P. Macquet, J.L. Butour, A circular dichroism study of DNA - platinum complexes, Eur. J. Biochem. 83 (1978) 375–385.
[58] M.V. Palmeira-Mello, A.B. Caballero, A. Lopez-Espinar, G.P. Guedes, A. Caubet, A. M.T. de Souza, M. Lanznaster, P. Gamez, DNA-interacting properties of two analogous square-planar cis-chlorido complexes: copper versus palladium, J. Biol. Inorg. Chem. 26 (2021) 727–740, https://doi.org/10.1007/s00775-021-01888-2.
[59] Z.F. Chen, M.X. Tan, Y.C. Liu, Y. Peng, H.H. Wang, H.G. Liu, H. Liang, Synthesis, characterization and preliminary cytotoxicity evaluation of five Lanthanide(III)-Plumbagin complexes, J. Inorg. Biochem. 105 (2011) 426–434, https://doi.org/10.1016/j.jinorgbio.2010.12.003.
[60] O. Suss, L. Motiei, D. Margulies, Broad applications of thiazole orange in fluorescent sensing of biomolecules and ions, Molecules 26 (2021), https://doi.org/10.3390/MOLECULES26092828.
[61] X. Jiang, L.A. Fielding, H. Davis, W. Carroll, E.C. Lisic, J.E. Deweese, Inhibition of topoisomerases by metal thiosemicarbazone complexes, Int. J. Mol. Sci. (2023) 24, https://doi.org/10.3390/ijms241512010.